ARTICLES
https://doi.org/10.1038/s41928-021-00595-9

nature electronics

Check for updates

Integration of boron arsenide cooling substrates into gallium nitride devices

Joon Sang Kang[1,3], Man Li[1,3], Huan Wu[1,3], Huuduy Nguyen[1,3], Toshihiro Aoki[2] and Yongjie Hu[1]✉

Thermal management is critical in modern electronic systems. Efforts to improve heat dissipation have led to the exploration of novel semiconductor materials with high thermal conductivity, including boron arsenide (BAs) and boron phosphide (BP). However, the integration of such materials into devices and the measurement of their interface energy transport remain unexplored. Here, we show that BAs and BP cooling substrates can be heterogeneously integrated with metals, a wide-bandgap semiconductor (gallium nitride, GaN) and high-electron-mobility transistor devices. GaN-on-BAs structures exhibit a high thermal boundary conductance of 250 MW m^{-2} K^{-1}, and comparison of device-level hot-spot temperatures with length-dependent scaling (from 100 μm to 100 nm) shows that the power cooling performance of BAs exceeds that of reported diamond devices. Furthermore, operating AlGaN/GaN high-electron-mobility transistors with BAs cooling substrates exhibit substantially lower hot-spot temperatures than diamond and silicon carbide at the same transistor power density, illustrating their potential for use in the thermal management of radiofrequency electronics. We attribute the high thermal management performance of BAs and BP to their unique phonon band structures and interface matching.

In most electronic systems, large amounts of waste heat are dissipated from hot spots to heat sinks across a series of device layers and interfaces that have a thermal resistance. A large thermal resistance—and hence rising hot-spot temperatures—can degrade device operation, so thermal management is an important technological challenge in the semiconductor industry[1–3]. Recent research on improving heat dissipation has focused on replacing common substrates (such as silicon carbide, silicon and sapphire) with high-thermal-conductivity (HTC) materials to reduce the overall thermal resistance[4–11]. A key challenge for high-performance thermal management is to achieve the combination of HTC with a low thermal boundary resistance (TBR—the resistance of an interface to thermal flow) near electronics junctions[3].

Diamond is currently the leading research prototype HTC material for high-performance power electronics cooling. It has been studied with wide-bandgap semiconductors and shown reduced hot-spot temperatures in gallium nitride (GaN)–diamond devices compared with traditional radiofrequency (RF) systems. However, GaN–diamond interfaces have poor TBR, which compromises the application potential of diamond for thermal management[3]. Conventional HTC materials have also been limited by their thermal properties and other intrinsic issues. For example, diamond and cubic boron nitride are challenging for applications because of their high-temperature and high-pressure synthesis requirements, slow growth rate, high cost, degraded quality and difficulty integrating with semiconductors. Graphite is highly anisotropic and mechanically soft due to having weak cross-plane van der Waals bonding. Nanomaterials such as graphene and nanotubes can be good conductors for individual materials, but, when integrated at practical sizes, their thermal conductivity degrades due to ambient interactions and disorder scattering.

Recently, new compound semiconductors[7–11] have been developed experimentally based on ab initio theory[12–20] and exhibit high thermal conductivity beyond that of most common heat conductors. In particular, an isotropic thermal conductivity of 500 W m^{-1} K^{-1} has been reported in boron phosphide (BP, ref. [7]) and 1,300 W m^{-1} K^{-1} in boron arsenide (BAs, refs. [8,11]). BAs has a thermal conductivity over three times that of industrial HTC standards such as copper and silicon carbide (SiC)—both around 400 W m^{-1} K^{-1}—and twice that of cubic boron nitride. Furthermore, the mechanical and thermophysical properties of BAs have been measured to be highly compatible with power semiconductors[11], as desired for device integration. The heterogeneous integration and characterization of BAs and BP with other material layers is critical to achieving their future implementation in devices for thermal management applications, but these remain unexplored.

In this Article, we report the interface characterization and integration of BAs and BP with other metal and semiconductor materials. We examine the heat dissipation performance and mechanisms at these interfaces via material characterizations, spectroscopy measurements and atomistic phonon transport theory simulations. Because of their unique phonon band structures, BAs and BP show a combination of high HTC and low TBR. Here, we develop GaN-on-BAs structures using metamorphic heteroepitaxy and measure a thermal boundary conductance of 250 MW m^{-2} K^{-1}. In the following, we highlight the potential of BAs as an alternative cooling substrate to diamond and other state-of-the-art HTC materials by using experimental data from GaN–BAs structures with a variable-width heat source to determine and investigate hot-spot temperatures of GaN transistors as a function of length scaling (from 100 μm to 100 nm) in both diffusive and ballistic transport regimes. We also develop device integration and provide experimental measurements of operational AlGaN/GaN high-electron-mobility transistors (HEMTs), verifying the superior cooling performance of BAs and showing its substantially lower hot-spot temperature (~60 K) than diamond (~110 K) and SiC (~140 K) at the same transistor power density.

Thermal management using BAs and BP cooling substrates

TBR is limited by the scattering of energy carriers from both sides of the interface[4,21,22] and has been shown to exist at all heterogeneous

[1]School of Engineering and Applied Science, University of California, Los Angeles, Los Angeles, CA, USA. [2]Irvine Materials Research Institute, Irvine, CA, USA. [3]These authors contributed equally: Joon Sang Kang, Man Li, Huan Wu, Huuduy Nguyen. ✉e-mail: yhu@seas.ucla.edu

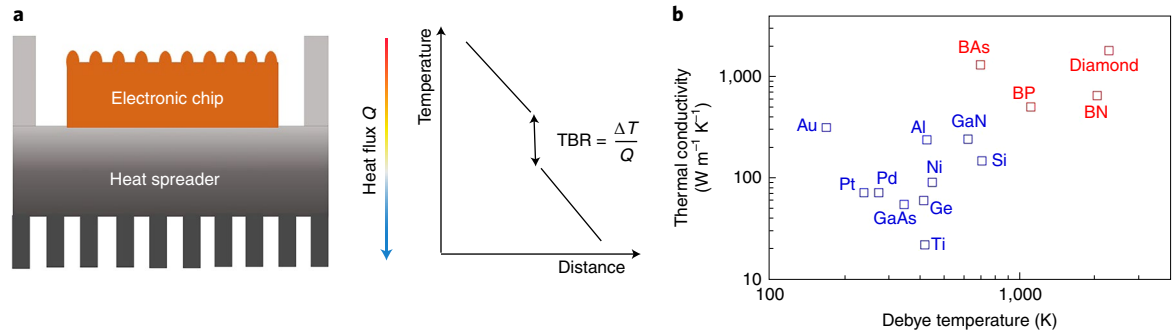

Fig. 1 | Electronics thermal management using integrated HTC materials as a cooling substrate to improve heat dissipation. a, Schematic illustrating heat dissipation and thermal boundary resistance (TBR) at the interfaces in microchip packaging. TBR = $\Delta T/Q$, where ΔT and Q are the temperature drop and heat flux across the interface, respectively. **b**, Room-temperature thermal conductivities and Debye temperatures of representative metals, semiconductors and HTC materials.

interfaces, regardless of atomic perfection. Despite improvements in material quality, such as surface roughness and defects[4,23], the ultimate limit of TBR for semiconductor device interfaces is usually dominated by the mismatch of atomistic vibrations (the modes of which are defined as phonons[21]) across the interface (Fig. 1a). Under the classical Debye approximation, the vibrational properties of materials are approximated by linear phonon dispersion, and the maximum temperature of the highest phonon frequency is defined as the Debye temperature (Θ_D)[24]. A simple metric to qualitatively evaluate the overlap between phonon spectra of two materials is to compare their Θ_D values (ref. [22]), where a smaller difference in Θ_D across the interface will be expected to result in a smaller TBR. Figure 1b compares Θ_D values for typical semiconductors, metals and HTC materials.

Most semiconductors (such as silicon, germanium, GaAs and GaN) and metals have Θ_D values below 700 K, while prototype HTC materials such as diamond and cubic BN have much higher values of Θ_D (over 2,000 K) due to their large phonon group velocity. It is therefore expected, and studies have confirmed, that there is a large TBR for diamond and BN interfaces after integration with typical semiconductors, which substantially compromises their application potential for thermal management, despite their high thermal conductivities. For example, the interface between diamond and GaN has a mismatch in Θ_D of over 1,500 K, resulting in a TBR of ~30 $m^2 K GW^{-1}$ (refs. [25–27]). By comparison, BAs and BP have much lower Θ_D values (for example, BAs has a Θ_D of ~700 K), suggesting they may show improved TBR upon integration.

Ultrafast spectroscopy for thermal transport measurements

Thermal transport was measured using ultrafast pump–probe spectroscopy based on the time-domain thermoreflectance (TDTR) technique, as illustrated in Fig. 2a. TDTR is well suited for this, as it requires no physical contact with the sample and the measurement can determine the TBR precisely[8,23,28,29]. In our set-up, a femtosecond-pulse laser with repetition rate of 80 MHz is generated by a Ti:sapphire optical cavity and divided into pump and probe beams. The pump beam doubles its frequency (a wavelength of 400 nm) after passing through a second harmonic generator, and is used to thermally excite the sample surface. The probe beam, at a wavelength of 800 nm, is used to detect the sample temperature. The time delay between pump and probe beams is precisely controlled by a mechanical delay stage with subpicosecond resolution. To determine the TBR, the transient TDTR signal is detected and fitted to a multilayer thermal model (Fig. 2c).

First, we measured the thermal transport across the interfaces of the HTC materials with various metals. Aluminium, gold, nickel, palladium, platinum and titanium films were deposited on top of BAs and BP thin films by electron-beam evaporation to form a clean metal–HTC interface, as verified by cross-sectional scanning electron microscopy (SEM; Fig. 2b). Our measurements of the temperature-dependent thermal boundary conductance (G, the reciprocal value of TBR) are shown in Fig. 2d,e. In general, metal interfaces with BAs and BP are measured to have high thermal conductance. The value of G varies for each metal but has a similar trend for BAs and BP. For example, gold and titanium have the lowest and highest G values, respectively. The measured thermal boundary conductance values (at room temperature) between BAs and gold, platinum, aluminium, palladium, nickel and titanium are 85, 133, 250, 290, 309 and 310 MW $m^{-2} K^{-1}$, respectively. These values are slightly higher than those obtained with BP, as expected from the difference in Θ_D. From 300 K to 600 K, no substantial temperature dependence is observed for G, indicating that complete phonon excitation and a saturated phonon population are involved in the interface transport. The thermal boundary conductances of BAs and BP with metals are typically over 4× and 2.5× higher, respectively, than those of a metal–diamond interface[30], verifying their high heat dissipation efficiency.

Ab initio calculations and MD simulations of interface energy transport

To understand the experimental results, we performed atomistic calculations to understand the phonon spectral contributions to the interfacial energy transport. Under the phonon picture, TBR can be understood as resulting from the breakdown of coherence of mode-dependent phonon transport across the interfaces[22]. As illustrated in Fig. 3a, when the incident phonons encounter the interface, partial transmission and partial reflection back could occur, but with different probabilities for each phonon mode. In most literature, for simplicity, the dispersion relationship is usually approximated by a linear dispersion relationship (the Debye approximation). However, the Debye approximation oversimplifies the TBR calculation, using a single phonon group velocity along each direction[31]. Here, we performed ab initio calculations[14,15,23,29] based on density functional theory (DFT) to obtain the full phonon band structures of the different materials (Fig. 3b), and constructed phonon-mode-dependent modelling of the interfacial thermal transport. The second-order interatomic force constants were calculated using the finite displacement method. For all the materials considered here, the projector augmented wave pseudopotential with the local density approximation was used. For each structure, a supercell with a 3×3×3 cubic unit cell with periodic condition was constructed for DFT calculations using the Quantum ESPRESSO package[32]. A 12×12×12 Monkhorst–Pack mesh was used for the

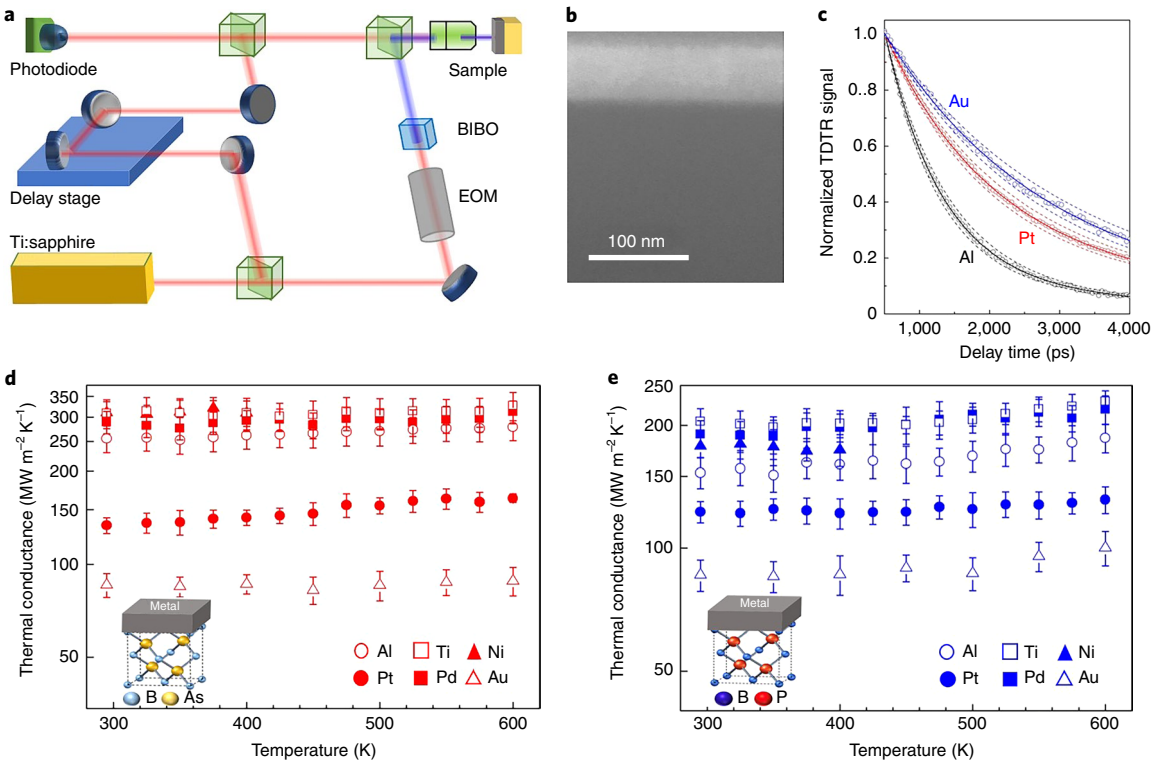

Fig. 2 | Heterogeneous interfaces and ultrafast optical spectroscopy measurements of temperature-dependent thermal boundary conductance. a, Schematic of the TDTR measurement set-up. Blue and orange routes represent pump and probe laser beams, respectively. EOM, electro-optic modulator; BIBO, bismuth borate. **b**, BAs and BP act as a cooling substrate for metal films. A cross-sectional SEM image of a typical sample is shown. The top layer is aluminium film and the bottom layer is BAs. **c**, Typical TDTR experimental data versus time (open circles), fitted to the thermal transport model (solid lines). Calculated curves (dashed lines) are shown with the thermal boundary conductance changed by ±10% of the best values to illustrate measurement accuracy. **d**,**e**, Experimental results for the temperature-dependent thermal boundary conductance between a range of metals and BAs (**d**) or BP (**e**). Error bars indicate the standard deviations of measurements.

reciprocal space, and the kinetic-energy cutoff for the plane-wave basis set was 600 eV. By displacing the atoms with a finite distance of 0.03 Å, the second-order force constants were extracted with the phono3py package. Our calculated phonon band structures were compared with neutron scattering and Raman scattering experiments[8,33–36] and show good consistency (Fig. 3b).

The phonon density of states (PDOS) were also calculated and are plotted on the right side of Fig. 3b. Note that the PDOS defines the number of available quantum states for each phonon energy. The PDOS overlap across the interface dictates TBR, as it determines the probability to prepare phonons before being incident on the interface and to accommodate phonons after transmission from the interface. Therefore, a larger PDOS overlap qualitatively indicates a lower TBR. The results in Fig. 3b show that the dominant range of the PDOS spans from 15 to 40 THz for diamond and from 0 to 20 THz for BAs or BP. By comparison, the PDOS is mainly distributed between 0 and 10 THz for most metals. In particular, the cutoff acoustic frequencies are 32.0 THz in diamond, 16.1 THz in BP, 9.6 THz in BAs, 9.5 THz in aluminium, 6.1 THz in platinum and 4.9 THz in gold. These PDOS spectra show that BAs overlaps best with most metals, followed by BP. Diamond is the option with the least overlap. The PDOS comparison further explains the improved TBR with BAs and BP versus diamond, as well as the variation between different metals, which is consistent with the experimental results shown in Fig. 2d,e.

To understand the fundamental limit of the TBR, we developed analytical calculations by taking advantage of our ab initio derived phonon band structures. Under the Landauer–Büttiker formulation[37,38], the TBR is calculated based on the mode-dependent properties as

$$\frac{1}{\mathrm{TBR}} = G = \frac{1}{2(2\pi)^3}\sum_i \int_{\mathbf{k}}^{\text{whole } k \text{ space}} \tau_{12}(\mathbf{k},i)\hbar\omega(\mathbf{k},i)\,|\mathbf{v}(\mathbf{k},i)\cdot\mathbf{n}|\,\frac{\mathrm{d}f}{\mathrm{d}T}\mathrm{d}\mathbf{k} \quad (1)$$

where $\tau_{AB}(\mathbf{k},i)$, $\omega(\mathbf{k},i)$, $\mathbf{v}(\mathbf{k},i)$ and $f = \frac{1}{\exp\left(\frac{\hbar\omega(\mathbf{k},i)}{k_B T}\right)-1}$ are the transmission coefficient, frequency, group velocity and equilibrium Bose–Einstein distribution function of phonons with wavevector $\mathbf{k}$ and polarization i. $\mathbf{n}$ is the unit vector normal to the interface. The subscript indicates the material on side 1 or side 2 across the interface. The transmission coefficient term ($\tau_{12}(\mathbf{k},i)$) is a key parameter to quantify how many phonons are reflected or allowed to transmit through the interface, as illustrated in Fig. 3a. First, we consider the lower limit of TBR as when the transmission of all overlapping phonon modes reaches 100% (that is, the radiation limit)[39]. Under this radiation limit, the phonon transport is similar to radiation heat transfer between blackbodies, so all the emitted phonons from one side of the interface would be accepted by the absorption side once the state of phonons is allowed into the absorption side. Mathematically, the transmission coefficient would be unitary, that is, $\tau_{12}(\mathbf{k},i)=1$, if the frequency of the emitted phonon from side 1 is lower than the maximum phonon frequency in side 1. The maximum G values based on the radiation limit, plotted as dotted lines in Fig. 3c, are

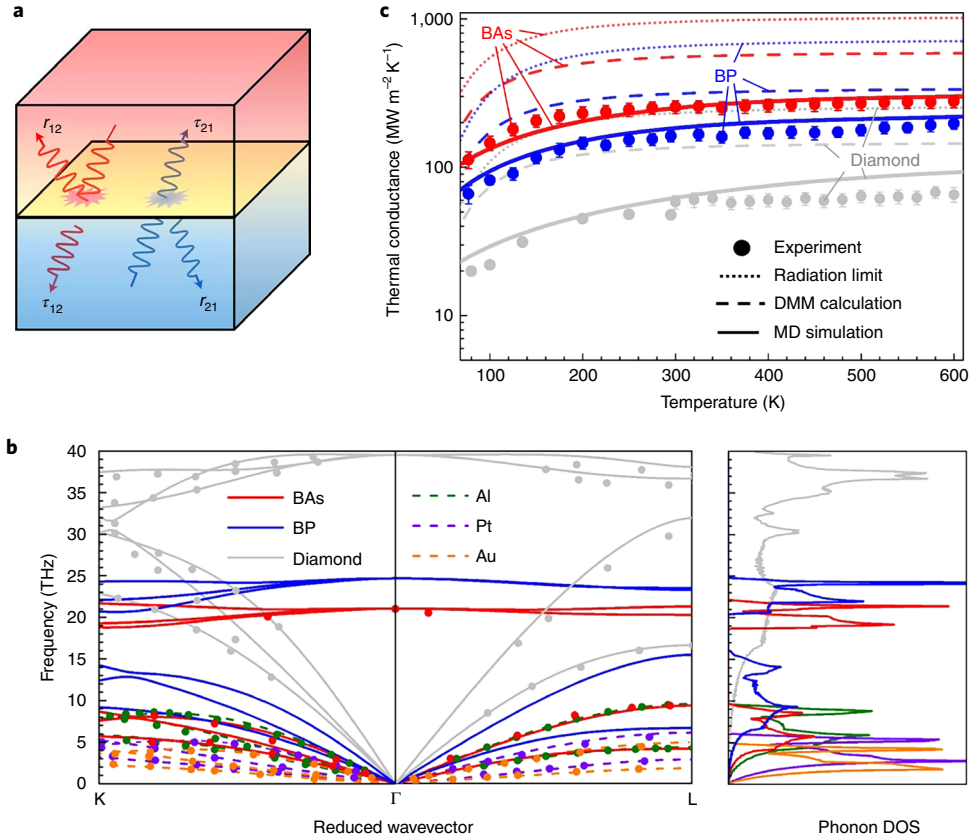

Fig. 3 | Ab initio calculation of phonon band structures and atomistic modelling of the phonon spectral contribution to the thermal boundary conductance. a, Schematic of phonon transport showing mode-specific transmission (τ) and reflection probability (r) at the interface. **b**, Phonon dispersion relationships (left) and density of states (right) of BAs, BP, diamond, aluminium (Al), platinum (Pt) and gold (Au) calculated using DFT (lines), in comparison with neutron scattering and Raman scattering experiments (dots[8,33–36]). **c**, Experimentally measured thermal boundary conductance (dots) of aluminium–HTC interfaces in comparison to calculations (lines), considering temperature dependence and different modelling methods.

953 MW m^{-2} K^{-1} for an Al–BAs interface, 652 MW m^{-2} K^{-1} for an Al–BP interface and 232 MW m^{-2} K^{-1} for an Al–diamond interface. As expected, the experimental results for the different interfaces follow the order predicted by the radiation limit, but the experimental values are far below this maximum limit, as full transmission cannot be achieved for practical interfaces. Alternatively, we consider the diffuse scattering limit of TBR under the diffuse mismatch model (DMM), where all the phonons lose their memory after scattering at the interface and, when re-emitted from the interface, can originally be from either side of the interface; that is, $\tau_{12}(\mathbf{k},i) = 1 - \tau_{21}(\mathbf{k},i)$. By applying this physical constraint and considering the detailed balance of heat flux[40], the transmission coefficient can be calculated as

$$\tau_{12}(\mathbf{k},i) = \frac{\sum_j \int_{\mathbf{k}}^{\mathrm{Side2}} |\mathbf{v}(\mathbf{k},j)\cdot\mathbf{n}|\delta_{\omega,\omega(\mathbf{k},j)}\,\mathrm{d}\mathbf{k}}{\sum_i \int_{\mathbf{k}}^{\mathrm{Side1}} |\mathbf{v}(\mathbf{k},i)\cdot\mathbf{n}|\delta_{\omega,\omega(\mathbf{k},i)}\,\mathrm{d}\mathbf{k} + \sum_j \int_{\mathbf{k}}^{\mathrm{Side2}} |\mathbf{v}(\mathbf{k},j)\cdot\mathbf{n}|\delta_{\omega,\omega(\mathbf{k},j)}\,\mathrm{d}\mathbf{k}} \quad (2)$$

where $\delta_{\omega,\omega(\mathbf{k},i)}$ is the Kronecker delta function. Note that the ab initio derived full phonon band structures from DFT calculations were used for the calculation, and the results for the interfaces between aluminium and BAs, BP and diamond are plotted as dashed lines in Fig. 3c. Both the above analytical calculation limits (the radiation limit and the diffuse scattering) show a consistent trend with the experimental measurements—that is, $G_{\mathrm{Al-BAs}} > G_{\mathrm{Al-BP}} > G_{\mathrm{Al-diamond}}$ over a wide (77–600 K) temperature range. In particular, the G values between BAs and metals are shown to be much larger than between diamond and metals due to the better match in the PDOS and the phonon group velocities from BAs. These analytical predictions are higher than the experimental results, as expected, because inelastic scattering processes and anharmonicity such as multiple phonons scattering need to be included to better describe the interface transport, as discussed in the following.

To better quantify the phonon scattering and interface energy transport, we calculated the TBR values using numerical simulations based on ab initio molecular dynamics (MD). We first developed the interatomic potentials for BAs and BP directly from quantum-mechanical calculations based on ab initio MD-determined atomic forces using the potfit package[41]. In the ab initio MD, Quantum ESPRESSO was used to construct a supercell with a 4×4×4 cubic unit cell for BAs and BP with norm-conserving pseudopotentials in the local-density approximation. The kinetic-energy cutoff for the plane-wave basis set was 1,360 eV. The Tersoff and embedded atom method potential were used for diamond and aluminium[42,43]. The interfacial interactions between aluminium and the HTC materials were described using the Lennard–Jones potential and the parameters were derived from the Lorentz–Berthelot rules[44,45]. To minimize mismatch at the interface, the supercell sizes were 10×10×80 (Al) and 11×11×80 (diamond) for the aluminium–diamond interface, 14×14×80 (aluminium) and 12×12×80 (BP) for the aluminium–BP interface and 13×13×80 (aluminium) and 11×11×80 (BAs) for the aluminium–BAs interface. The entire systems were relaxed under an isothermal–isobaric ensemble at the desired temperature and pressure for 5 ns, followed by relaxation under a canonical ensemble for 3 ns and microcanonical ensemble for 2 ns with a time step of 0.5 fs. MD simulations were performed with a large-scale atomic/molecular massively parallel simulator

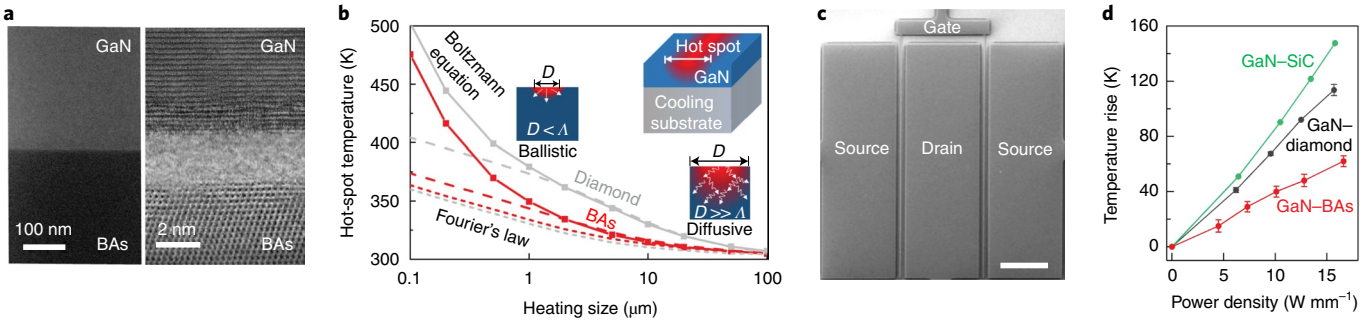

Fig. 4 | Device integration of BAs and GaN for high-performance thermal management versus transistor channel length scaling and power density. **a**, Cross-sectional SEM (left) and high-resolution TEM (right) images of a GaN–BAs structure, showing the atomically resolved interface. **b**, Simulations of the hot-spot temperatures for the two best thermal conductors (BAs and diamond), as a function of heating size (from 100 μm to 100 nm). Top right inset: schematics of transport physics and the simulation domain, including a 0.8-μm-thick GaN layer on top of a 100-μm-thick cooling substrate. All simulation inputs are from experimental measurements and ab initio calculations. A comparison of Fourier's heat conduction law (dashed lines) and the spectral-dependent Boltzmann transport equation (solid lines) quantifies the transition from diffusive to ballistic thermal transport (smaller insets). The size-dependent hot-spot temperature results indicate that BAs has a superior performance for nanoscale thermal management due to both its high thermal conductivity and thermal boundary conductance. **c**,**d**, Experimental measurements were made of the hot-spot temperature rise in operating AlGaN/GaN HEMTs as a function of transistor power density, with different cooling substrates (BAs, diamond and SiC). All devices shared the same geometry: two fingers, with a width of 100 μm and gate pitch of 34 μm. An SEM image of the fabricated HEMT device is shown in **c** (scale bar, 20 μm) and a plot of GaN temperature as a function of power density is shown in **d**, measured using Raman spectroscopy on the drain side at a lateral distance of 0.5 μm from the T-gate edge, for transistors on a GaN-on-BAs wafer, as well as a reference GaN-on-diamond wafer and GaN-on-SiC wafer. Data for diamond and SiC substrates are adapted from ref. [26].

(LAMMPS)[46]. By setting anchor layers and thermal reservoirs at the two ends of the system, the steady-state temperature profile across the system under a constant heat flux could be obtained after 10 ns. The TBR values were determined from the heat flux and temperature drop at the interface. The MD-predicted TBRs for the interface with BAs, BP and diamond are plotted in comparison with experimental results in Fig. 3c. The MD predictions are in closer agreement with the experimental measurements, indicating that a more realistic interatomic interaction that includes elastic phonon scattering, high-order anharmonicity and phonon mode conversion can better describe the phonon behaviour at the interface and that such atomistic interactions dictate the macroscopic TBRs. More importantly, the consistent trend between the radiation limit, phonon diffuse scattering and MD simulation supports the conclusion that the unique band structure of BAs facilitates efficient phonon transport across the interface and ensures that its TBR is intrinsically low.

Heterogeneous integration of BAs–GaN structures

We next demonstrate the experimental integration of BAs with a prototype high-power semiconductor, GaN, and measure the heat dissipation performance. Recent progress[25–27,47–51] has been made in integrating GaN with classical HTC materials (in particular, diamond and SiC) for power cooling, with a focus on improving the near-junction lattice mismatch, defects and the resulting TBR (which limits the overall heat dissipation). To directly integrate BAs with GaN is challenging, because the crystal structures of BAs (zinc blende cubic) and GaN (wurtzite) are different, making it difficult to form epitaxial interfaces with minimum disorder. Also, BAs decomposes at ~1,200 K, so low-temperature crystal growth is required. To obtain a high-quality interface between BAs and GaN, a metamorphic heteroepitaxy method was thus used to relax the strain[52], with a thin layer of oxide introduced between them as an adhesion layer, using an atomic layer deposition technique[53]. A follow-up oxygen plasma treatment was then used to activate interface bonds and the sample was annealed at 773 K for 24 h in vacuum. The heterogeneous interface was verified by SEM and high-resolution transmission electron microscopy (HR-TEM). Figure 4a shows an atomically clean and uniform GaN–BAs interface with a 2-nm interlayer aluminium oxide. The thermal boundary conductance of the high-quality BAs–GaN interface was measured using TDTR as ~250 MW m^{-2} K^{-1}, which is over eight times higher than that of typical GaN–diamond interfaces[25–27]. Moreover, considering that the oxide layer could serve as a barrier to scatter phonons and introduce an additional series resistance (~1.4 m^2 K GW^{-1} for 2-nm oxide, or 35% of the measured total resistance), the TBR of the GaN–BAs interface could be subject to further enhancement through optimization of the resistance contribution from the oxide interlayer.

Multiscale power cooling and device length scaling

To evaluate the device-level heat dissipation performance of BAs as a cooling substrate, we determined the hot-spot temperature across a GaN–BAs interface as a function of various heating sizes from 100 μm to 100 nm (Fig. 4b). The heat dissipation performance of the GaN–BAs device was compared with that of a current state-of-the-art GaN–diamond device. We considered an example device geometry involving a GaN device layer on top of a BAs or diamond cooling substrate by using experimental data as the input and solving the heat conduction equation and the Boltzmann transport equation (BTE; top right inset, Fig. 4b). A boundary line heat source with fixed power (for example, 10 W mm^{-1}) was placed on top of the GaN layer to serve as the hot spot, and the bottom of the substrate was fixed at room temperature. To study the size-dependent effect of the hot-spot temperature, the width of the heat source was varied. Experimental data for the TBR and thermal conductivity were used for these simulations.

We first simulated a hot-spot temperature by solving the heat conduction equation using the finite-element method. In this case, thermal transport is considered as a diffusive process, where the heat flux is proportional to the temperature gradient (following Fourier's heat conduction law). Classical diffusion theory describes the thermal transport process well when the characteristic length is far larger than the phonon mean free path, and is commonly used for engineering macroscopic devices. The hot-spot temperature increases when the heater width decreases, due to the larger heating power density. To evaluate the effect from TBR, by intentionally removing TBR in the simulation (dotted lines), we found

that, as expected due to its high thermal conductivity, diamond shows a slight advantage. However, when TBR is included in the simulation (dashed lines), which is the case for practical devices, BAs has a much lower hot-spot temperature than diamond, supporting its superior performance in heat dissipation through the combination of a high HTC and low TBR.

We also evaluated the device performance under conditions where ballistic transport takes place and classical diffusion theory fails for nanoscale devices[20]. On shrinking device sizes below the phonon mean free paths, phonon transport will not experience scattering. In this case, practical heat dissipation behaves more like radiation than diffusion, so the actual hot-spot temperature will deviate from the prediction of Fourier's law. The ballistic thermal transport and phonon mean free path spectra of GaN, diamond, BAs and BP have all been experimentally measured and analysed in our recent studies[7,8,20]. Here, to capture the physics of thermal transport from the diffusive regime to the ballistic regime, we solved the spectral-dependent BTE considering mode-dependent phonon properties for the same device structure. The three-dimensional (3D) spectral-dependent BTE is given by

$$\frac{\partial f}{\partial t} + \mathbf{v}(\omega, i) \cdot \nabla f = -\frac{f - f_0}{\boldsymbol{\tau}(\omega, i)} \quad (3)$$

where f is the phonon distribution function, f_0 is the equilibrium Bose–Einstein distribution at the local temperature, and $\mathbf{v}(\omega,i)$ and $\boldsymbol{\tau}(\omega,i)$ are, respectively, the phonon group velocity and the phonon relaxation time at a certain angular frequency ω and polarization i. $\Lambda = v\tau$ is the phonon mean free path. For the multiscale simulation, because it is, in general, very challenging to solve the 3D spectral-dependent BTE, especially using deterministic methods, we here deploy a recently developed variance-reduced Monte Carlo (VRMC) method[7] to solve the BTE for the 3D experimental geometry. In the VRMC method, phonon bundles are initialized in the computational domain, and then proceed following 'advection–sampling–scattering' procedures[54]. In the advection procedure, the phonon bundles are moved under group velocity. In the sampling procedure, the energy carried by the phonon bundles is sampled. In the scattering procedure, the frequencies of the phonon bundles are redistributed based on the spectral distribution of the specific heat. To determine the hot-spot temperature, we calculate the temperature response to a heat pulse and integrate the response from $t = 0$ to infinity. All the material's spectral properties for the input into the BTE simulation come from ab initio calculations and experiments.

Figure 4b shows the hot-spot temperature as a function of the scaling heating sizes. As expected, on reducing the heating width from 100 µm to 100 nm, the hot-spot temperature increases due to the increased packing density. We also notice that the ballistic heat transfer becomes substantial for heat spots of small sizes, so the Fourier's law result (dashed line) deviates significantly from the BTE calculation (solid line), that is, representing practical heating behaviour. When the heating width is large, the results of Fourier's law are consistent with the BTE, but when the heating source width is smaller than 1 µm, the hot-spot temperature from the BTE is much higher than with Fourier's law; this difference between the BTE and Fourier's law results increases dramatically as the width of the heating source decreases. Fundamentally, ballistic transport takes place when the heated spot size is smaller than the mean free paths, and here it occurs for a heating source width on the order of ~1 µm, which is consistent with our previous study of phonon mean free paths[7,8,20]. The result shows that, at the nanoscale, ballistic transport will substantially increase the overheating issue over classical theory prediction.

The hot-spot temperatures are compared for the GaN–BAs device and the state-of-the-art GaN–diamond device in Fig. 4b. This clearly shows that, for the whole range of scaling lengths, BAs has improved heat dissipation performance compared with diamond. For example, with a 1-µm heating width, the hot-spot temperature for BAs is 38% lower than that of diamond (currently the best reported in the literature for high-power cooling[3]). The results demonstrate that the high G value between GaN and BAs (250 MW m^{-2} K^{-1}), together with the high thermal conductivity of BAs (1,300 W m^{-1} K^{-1}), substantially improve heat dissipation compared to other state-of-the-art HTC materials.

Device integration and in situ measurement of AlGaN/GaN HEMTs

Finally, we carried out device integration with HEMTs and experimentally measured the operating HEMT devices for a comparison of the performances of the BAs, diamond and SiC cooling substrates. To make a fair comparison, the HEMTs were fabricated using the same AlGaN/GaN epitaxial layers and device layout (Methods). Figure 4c presents an SEM image of our fabricated HEMTs device integrated on top of a BAs substrate. In Fig. 4d, we show the hot-spot temperature rise, while operating the AlGaN/GaN HEMTs, as a function of power density for the different cooling substrates. With the same device layout and operating conditions, the device cooling performance for BAs exceeds that for diamond and SiC, verifying the modelling predictions. For example, at a transistor power density of ~15 W mm^{-1}, the hot-spot temperature rise is ~60 K for GaN–BAs, substantially lower than the temperature rise for GaN–diamond (~110 K) and GaN–SiC (~140 K) devices.

Conclusions

We have reported the heterogeneous integration of BAs and BP as HTC cooling substrates for high-performance thermal management. Metamorphic heteroepitaxy growth was used to fabricate BAs–GaN structures, and the thermal boundary conductance was found to offer an eightfold improvement compared with a typical diamond–GaN interface[25–27]. The hot-spot temperatures of GaN devices integrated with different cooling substrates were examined in diffusive and ballistic regimes with length scaling from 100 µm to 100 nm. Ultrafast spectroscopy measurements and atomistic theory calculations demonstrated that interface thermal transport is substantially improved with BAs and BP in comparison to reported state-of-the-art materials. The enhancement in heat dissipation is attributed, via ab initio and atomistic simulations, to the material's phonon band structures, considered under the radiation limit and diffuse scattering limit, as well as by ab initio MD simulations. Measurements of hot-spot temperatures of AlGaN/GaN HEMTs also showed reduced temperatures using BAs as a cooling substrate compared with diamond and SiC. Device integration of these HTC materials could improve future electronics packaging and extend the roadmap of high-power electronics.

Methods

HTC substrates and metal films. BP and BAs samples were synthesized by epitaxial growth and flux growth methods, respectively, as described in our previous reports[7,8]. The different metal films (Al, Au, Ni, Pd, Pt and Ti, Kurt J. Lesker Company, 99.999%) were deposited on the samples using an electron-beam evaporator under high vacuum (~10^{-7} torr) with a deposition rate of ~1 Å s^{-1}.

Heteroepitaxy integration of BAs and GaN. GaN samples including both bare GaN film and AlGaN/GaN HEMTs were integrated with BAs for the study. A thin oxide layer was deposited on each surface of the BAs and GaN samples using atomic layer deposition (Fiji F200, Cambridge Nanotech). Trimethylaluminium was used as precursor to deposit 10 cycles of Al_2O_3 at 473 K. Oxygen plasma treatment was applied to the oxide layers. More process details are provided in ref. [55]. BAs and GaN samples were mechanically transferred and bonded together via the oxide layers. The bonded BAs–GaN samples were annealed at 773 K in vacuum to form the high-quality interfaces for measurements. To examine the thermal stability, the integrated samples were measured with thermal cycling between room temperature and 600 K more than 10 times. All the samples were measured with consistent results and no appreciable degradation.

AlGaN/GaN–BAs HEMT devices. A GaN-on-Si wafer consisting of an ~1-μm-thick AlGaN transition layer, 1-μm-thick GaN buffer layer and 20-nm AlGaN top barrier layer was used as the device layer. HEMT devices with two fingers (100-μm-wide and 34-μm gate pitch) were fabricated using electron-beam lithography (JSM-6610, JEOL). Rapid thermal annealing (RTA, RTP 600xp, Modular Process Technology) at 973 K for 30 s under forming gas (98% argon and 2% hydrogen) was used to form ohmic contacts. The Si substrate and AlGaN epitaxial transition layer, used to accommodate the lattice mismatch during GaN-on-Si growth, were selectively etched out using an HNO_3:HF:CH_3COOH (5:4:1) mixture and AZ400K developer, respectively. The exposed clean and smooth GaN surface was bonded with the BAs substrate following the heteroepitaxy integration process. The HEMT epitaxial layers, device layout, *I*–*V* characteristics and operation conditions for GaN–BAs are consistent with the reported GaN–diamond and GaN–SiC devices[26]. More details regarding transistor fabrication and electrical transport characterizations are provided in previous reports[56–60].

TEM measurements. TEM samples of BAs and GaN heterostructures were prepared using a focused ion beam (FIB) machine (Nova 600, FEI). The sample was cut by FIB into small pieces (5 μm × 5 μm × 2 μm, width × height × thickness) and transferred to a TEM sample holder (PELCO FIB Lift-Out, Ted Pella) with a nanomanipulator. The heterostructure sample was further milled by FIB until the sample thickness was thin enough (<100 nm) to be traversed by the electron beam for effective TEM imaging. After FIB, the sample was transferred to an aberration-corrected scanning TEM instrument (Grand ARM, JEOL) for imaging. Annular bright-field images were taken under a 300-keV acceleration voltage. The measured data and atomic-resolution TEM images were processed with Gatan TEM software.

Raman spectroscopy. Raman thermography was performed using micro Raman spectroscopy (inVia, Renishaw) under 488-nm laser excitation with a 2,400-mm^{-1} grating. The laser was polarized and backscattered with a Leica DM2500 optical system. We used a ×50/0.75-numerical-aperture objective lens, and the measured lateral spatial resolution was 0.5 μm. In addition, calibrations of the temperature, thermoelastic stress and electrical field in the GaN HEMTs were carefully performed according to recent literature[61,62] to determine accurate temperatures via Raman measurements.

Data availability

The data that support the plots within this paper and the other findings of this study are available from the corresponding author upon reasonable request.

Received: 30 June 2020; Accepted: 5 May 2021;
Published online: 17 June 2021

References

1. Waldrop, M. M. The chips are down for Moore's law. *Nature* **530**, 144–147 (2016).
2. Ball, P. Computer engineering: feeling the heat. *Nature* **492**, 174–176 (2012).
3. ITRS. *International Technology Roadmap for Semiconductors 2.0*: *Executive Report* 79 (Semiconductor Industry Association, 2015).
4. Cui, Y., Li, M. & Hu, Y. Emerging interface materials for electronics thermal management: experiments, modeling and new opportunities. *J. Mater. Chem. C* **8**, 10568 (2020).
5. Bubnova, O. Thermal release. *Nat. Nanotechnol.* **13**, 620 (2018).
6. Cui, Y., Qin, Z., Wu, H., Li, M. & Hu, Y. Flexible thermal interface based on self-assembled boron arsenide for high-performance thermal management. *Nat. Commun.* **12**, 1284 (2021).
7. Kang, J. S., Wu, H. & Hu, Y. Thermal properties and phonon spectral characterization of synthetic boron phosphide for high thermal conductivity applications. *Nano Lett.* **17**, 7507–7514 (2017).
8. Kang, J. S., Li, M., Wu, H., Nguyen, H. & Hu, Y. Experimental observation of high thermal conductivity in boron arsenide. *Science* **578**, 575–578 (2018).
9. Li, S. et al. High thermal conductivity in cubic boron arsenide crystals. *Science* **581**, 579–581 (2018).
10. Tian, F. et al. Unusual high thermal conductivity in boron arsenide bulk crystals. *Science* **585**, 582–585 (2018).
11. Kang, J. S., Li, M., Wu, H., Nguyen, H. & Hu, Y. Basic physical properties of cubic boron arsenide. *Appl. Phys. Lett.* **115**, 122103 (2019).
12. Lindsay, L., Broido, D. A. & Reinecke, T. L. First-principles determination of ultrahigh thermal conductivity of boron arsenide: a competitor for diamond? *Phys. Rev. Lett.* **111**, 025901 (2013).
13. Broido, D. A., Lindsay, L. & Reinecke, T. L. Ab initio study of the unusual thermal transport properties of boron arsenide and related materials. *Phys. Rev. B* **88**, 214303 (2013).
14. Wu, H., Fan, H. & Hu, Y. Ab initio determination of ultrahigh thermal conductivity in ternary compounds. *Phys. Rev. B* **103**, L041203 (2021).
15. Fan, H., Wu, H., Lindsay, L. & Hu, Y. Ab initio investigation of single-layer high thermal conductivity boron compounds. *Phys. Rev. B* **100**, 085420 (2019).
16. Feng, T., Lindsay, L. & Ruan, X. Four-phonon scattering significantly reduces intrinsic thermal conductivity of solids. *Phys. Rev. B* **96**, 161201(R) (2017).
17. Mingo, N. & Broido, D. A. Lattice thermal conductivity crossovers in semiconductor nanowires. *Phys. Rev. Lett.* **93**, 246106 (2004).
18. Ward, A., Broido, D. A., Stewart, D. A. & Deinzer, G. Ab initio theory of the lattice thermal conductivity in diamond. *Phys. Rev. B* **80**, 125203 (2009).
19. Esfarjani, K., Chen, G. & Stokes, H. T. Heat transport in silicon from first-principles calculations. *Phys. Rev. B* **84**, 085204 (2011).
20. Hu, Y., Zeng, L., Minnich, A. J., Dresselhaus, M. S. & Chen, G. Spectral mapping of thermal conductivity through nanoscale ballistic transport. *Nat. Nanotechnol.* **10**, 701–706 (2015).
21. Ziman, J. M. *Electrons and Phonons*: *The Theory of Transport Phenomena in Solids* (Oxford Univ. Press, 1960).
22. Swartz, E. T. & Pohl, R. O. Thermal boundary resistance. *Rev. Mod. Phys.* **61**, 605–668 (1989).
23. Li, M., Kang, J. S. & Hu, Y. Anisotropic thermal boundary resistance across two-dimensional black phosphorous: experiment and atomistic modeling of interfacial energy transport. *Adv. Mater.* **31**, 1901021 (2019).
24. Kittel, C. *Introduction to Solid State Physics* (Wiley, 1976).
25. Cho, J. et al. Improved thermal interfaces of GaN–diamond composite substrates for HEMT applications. *IEEE Trans. Compon. Packag. Manuf. Technol.* **3**, 79–85 (2013).
26. Pomeroy, J. W., Bernardoni, M., Dumka, D. C., Fanning, D. M. & Kuball, M. Low thermal resistance GaN-on-diamond transistors characterized by three-dimensional Raman thermography mapping. *Appl. Phys. Lett.* **104**, 083513 (2014).
27. Liu, D. et al. GaN-on-diamond electronic device reliability: mechanical and thermo-mechanical integrity. *Appl. Phys. Lett.* **107**, 251902 (2015).
28. Li, M., Kang, J. S. & Hu, Y. Anisotropic thermal conductivity measurement using a new asymmetric-beam time-domain thermoreflectance (AB-TDTR) method. *Rev. Sci. Instrum.* **89**, 084901 (2018).
29. Kang, J. S., Wu, H., Li, M. & Hu, Y. Intrinsic low thermal conductivity and phonon renormalization due to strong anharmonicity of single-crystal tin selenide. *Nano Lett.* **19**, 4941–4948 (2019).
30. Stoner, R. J., Maris, H. J., Anthony, T. R. & Banholzer, W. F. Measurements of the Kapitza conductance between diamond and several metals. *Phys. Rev. Lett.* **68**, 1563–1566 (1992).
31. Monachon, C., Weber, L. & Dames, C. Thermal boundary conductance: a materials science perspective. *Annu. Rev. Mater. Res.* **46**, 433–463 (2016).
32. Giannozzi, P. et al. QUANTUM ESPRESSO: a modular and open-source software project for quantum simulations of materials. *J. Phys. Condens. Matter* **21**, 395502 (2009).
33. Stedman, R. & Nilsson, G. Dispersion relations for phonons in aluminum at 80 and 300 °K. *Phys. Rev.* **145**, 492–500 (1966).
34. Sharma, P. K. & Singh, N. Phonon dispersion in noble metals. *Phys. Rev. B* **4**, 4636–4639 (1971).
35. Dutton, D. H., Brockhouse, B. N. & Miller, A. P. Crystal dynamics of platinum by inelastic neutron scattering. *Can. J. Phys.* **50**, 2915–2927 (1972).
36. Aggarwal, K. G. Lattice dynamics of diamond. *Proc. Phys. Soc.* **91**, 381–389 (1967).
37. Landauer, R. Spatial variation of currents and fields due to localized scatterers in metallic conduction. *IBM J. Res. Dev.* **1**, 223–231 (1957).
38. Büttiker, M., Imry, Y., Landauer, R. & Pinhas, S. Generalized many-channel conductance formula with application to small rings. *Phys. Rev. B* **31**, 6207–6215 (1985).
39. Snyder, N. S. Heat transport through helium II: Kapitza conductance. *Cryogenics* **10**, 89–95 (1970).
40. Chen, G. *Nanoscale Energy Transport and Conversion* (Oxford Univ. Press, 2005).
41. Brommer, P. et al. Classical interaction potentials for diverse materials from ab initio data: a review of potfit. *Model. Simul. Mater. Sci. Eng.* **23**, 074002 (2015).
42. Erhart, P. & Albe, K. Analytical potential for atomistic simulations of silicon, carbon and silicon carbide. *Phys. Rev. B* **71**, 035211 (2005).
43. Jacobsen, K. W., Norskov, J. K. & Puska, M. J. Interatomic interactions in the effective-medium theory. *Phys. Rev. B* **35**, 7423–7442 (1987).
44. Delhommelle, J. & Millié, P. Inadequacy of the Lorentz–Berthelot combining rules for accurate predictions of equilibrium properties by molecular simulation. *Mol. Phys.* **99**, 619–625 (2001).
45. Rappé, A. K., Casewit, C. J., Colwell, K. S., Goddard, W. A. & Skiff, W. M. UFF, a full periodic table force field for molecular mechanics and molecular dynamics simulations. *J. Am. Chem. Soc.* **114**, 10024–10035 (1992).
46. Plimpton, S. Fast parallel algorithms for short-range molecular dynamics. *J. Comput. Phys.* **117**, 1–19 (1997).

47. Cho, J., Li, Z., Asheghi, M. & Goodson, K. Near-junction thermal management: thermal conduction in gallium nitride composite substrates. *Annu. Rev. Heat Transf.* **18**, 7–45 (2015).
48. Cho, J., Francis, D., Altman, D. H., Asheghi, M. & Goodson, K. E. Phonon conduction in GaN–diamond composite substrates. *J. Appl. Phys.* **121**, 055105 (2017).
49. Zhou, Y. et al. Barrier-layer optimization for enhanced GaN-on-diamond device cooling. *ACS Appl. Mater. Interfaces* **9**, 34416–34422 (2017).
50. Yates, L. et al. Low thermal boundary resistance interfaces for GaN-on-diamond devices. *ACS Appl. Mater. Interfaces* **10**, 24302–24309 (2018).
51. Cheng, Z., Mu, F., Yates, L., Suga, T. & Graham, S. Interfacial thermal conductance across room-temperature-bonded GaN/diamond interfaces for GaN-on-diamond devices. *ACS Appl. Mater. Interfaces* **12**, 8376–8384 (2020).
52. Ayers, J. E. *Heteroepitaxy of Semiconductors*: *Theory*, *Growth and Characterization* (CRC Press, 2007).
53. Hu, Y., Kuemmeth, F., Lieber, C. M. & Marcus, C. M. Hole spin relaxation in Ge–Si core–shell nanowire qubits. *Nat. Nanotechnol.* **7**, 47–50 (2012).
54. Péraud, J.-P. M. & Hadjiconstantinou, N. G. An alternative approach to efficient simulation of micro/nanoscale phonon transport. *Appl. Phys. Lett.* **101**, 153114 (2012).
55. Hu, Y. et al. A Ge/Si heterostructure nanowire-based double quantum dot with integrated charge sensor. *Nat. Nanotechnol.* **2**, 622–625 (2007).
56. Ke, M. et al. Complementary doping of van der Waals materials through controlled intercalation for monolithically integrated electronics. *Nano Res.* **13**, 1369–1375 (2020).
57. Nguyen, H. D., Kang, J. S., Li, M. & Hu, Y. High-performance field emission based on nanostructured tin selenide for nanoscale vacuum transistors. *Nanoscale* **11**, 3129–3137 (2019).
58. Hu, Y., Xiang, J., Liang, G., Yan, H. & Lieber, C. M. Sub-100 nanometer channel length Ge/Si nanowire transistors with potential for 2-THz switching speed. *Nano Lett.* **8**, 925–930 (2008).
59. Xiang, J. et al. Ge/Si nanowire heterostructures as high-performance field-effect transistors. *Nature* **441**, 489–493 (2006).
60. Brovman, Y. M. et al. Electric field effect thermoelectric transport in individual silicon and germanium/silicon nanowires. *J. Appl. Phys.* **119**, 234304 (2016).
61. Choi, S., Heller, E. R., Dorsey, D., Vetury, R. & Graham, S. Thermometry of AlGaN/GaN HEMTs using multispectral raman features. *IEEE Trans. Electron Devices* **60**, 1898–1904 (2013).
62. Bagnall, K. R., Moore, E. A., Badescu, S. C., Zhang, L. & Wang, E. N. Simultaneous measurement of temperature, stress and electric field in GaN HEMTs with micro-Raman spectroscopy. *Rev. Sci. Instrum.* **88**, 113111 (2017).

Acknowledgements

We thank H. Albrecht for careful proofreading of this manuscript and P. Chen for helpful discussion. Y.H. acknowledges support from an Alfred P. Sloan Research Fellowship under grant no. FG-2019-11788, a CAREER Award from the National Science Foundation (NSF) under grant no. DMR-1753393, a Young Investigator Award from the United States Air Force Office of Scientific Research under grant no. FA9550-17-1-0149, the Watanabe Excellence in Research Award, the Sustainable LA Grand Challenge and the Anthony and Jeanne Pritzker Family Foundation. This work used computational and storage services associated with the Hoffman 2 Shared Cluster provided by UCLA Institute for Digital Research and Education's Research Technology Group, and the Extreme Science and Engineering Discovery Environment (XSEDE), which is supported by NSF under grant no. ACI-1548562.

Author contributions

Y.H. proposed and directed the research. J.S.K., M.L. and H.N. performed the experiments. M.L. and H.W. performed the theory calculations. T.A. helped with the TEM study. J.S.K., M.L., H.W., H.N. and Y.H. discussed the results and commented on the manuscript.

Competing interests

The authors declare no competing interests.

Additional information

Correspondence and requests for materials should be addressed to Y.H.

Peer review information *Nature Electronics* thanks Qian Zhang and the other, anonymous, reviewer(s) for their contribution to the peer review of this work.

Reprints and permissions information is available at www.nature.com/reprints.

Publisher's note Springer Nature remains neutral with regard to jurisdictional claims in published maps and institutional affiliations.

© The Author(s), under exclusive licence to Springer Nature Limited 2021